

# On the turbulence structure in inert and reacting compressible mixing layers

INGA MAHLE<sup>1</sup>, HOLGER FOYSI<sup>2</sup>,  
SUTANU SARKAR<sup>2</sup> AND RAINER FRIEDRICH<sup>1</sup>

<sup>1</sup>Fachgebiet Strömungsmechanik, Technische Universität München,  
Boltzmannstr. 15, 85748 Garching, Germany

<sup>2</sup>UC San Diego, 9500 Gilman Drive, La Jolla, CA 92093, USA

(Received 6 June 2007 and in revised form 27 September 2007)

Direct numerical simulation is used to investigate effects of heat release and compressibility on mixing-layer turbulence during a period of self-similarity. Temporally evolving mixing layers are analysed at convective Mach numbers between 0.15 and 1.1 and in a Reynolds number range of 15000 to 35000 based on vorticity thickness. The turbulence inhibiting effects of heat release are traced back to mean density variations using an analysis of the fluctuating pressure field based on a Green's function.

## 1. Introduction

A reduction in turbulence activity and in the growth rate of mixing layers when the convective Mach number,  $M_c$ , increases, are well-known phenomena. Even though it is known from experiments and simulations of reacting mixing layers (see Hermanson & Dimotakis 1989; McMurtry, Riley & Metcalfe 1989; Pantano, Sarkar & Williams 2003) that heat release due to combustion has similar effects, few examples, one being Miller, Bowman & Mungal (1998), can be found in literature treating both mechanisms, heat release and compressibility, simultaneously. This, however, has important implications for applications such as scramjet engines, the efficiency of which depends on a proper mixing of oxidizer and fuel.

Direct numerical simulation (DNS) studies by Vreman, Sandham & Luo (1996) and Freund, Lele & Moin (2000) show that, with increasing  $M_c$ , there is a decrease in pressure fluctuations leading to a reduction in pressure–strain terms, which is responsible for the decrease in growth rate. Pantano & Sarkar (2002) confirmed these results in their DNS and performed a supporting analysis based on the wave equation for the pressure fluctuations. In a reacting shear layer, heat release due to chemical reactions significantly decreases the mean density. Therefore, the role of mean density effects is of interest. Such effects were found to be key to the reduction of pressure–strain correlations in inert compressible channel flow (see Foysi, Sarkar & Friedrich 2004).

The relevance of mean density effects in shear layers is one focus of the present paper. Section 2 gives an overview of the simulations. In §3, the main part of the paper, averaged quantities are shown and analysed. Particular attention is given to the pressure–strain correlations which are computed with the help of a Green's function. In the last section, a summary is given and conclusions are drawn.

Case	$L_1/\delta_{\omega,0}$	$L_2/\delta_{\omega,0}$	$L_3/\delta_{\omega,0}$	$N_1$	$N_2$	$N_3$
Inert	192.375	32.25	96.75	768	192	576
Reacting	345	86	172	768	192	432

TABLE 1. Computational parameters:  $L_1$ ,  $L_2$ ,  $L_3$  are the streamwise, spanwise and transverse domain sizes resolved by  $N_1$ ,  $N_2$  and  $N_3$  grid points, respectively.  $\delta_{\omega,0}$  is the vorticity thickness of the shear layer at  $Re_{\omega,0} = 640$ . This Reynolds number is based on  $\delta_{\omega,0}$ ,  $\Delta u$ , and the average density/viscosity of the free streams.

## 2. DNS of inert and reacting compressible mixing layers

DNS of inert and reacting temporally evolving mixing layers are performed at three different convective Mach numbers ( $M_c = 0.15, 0.7$  and  $1.1$ ),  $M_c$  being based on the velocity difference across the layer,  $\Delta u$ , and the sum of free-stream sound speeds. Table 1 gives the computational parameters. The smoother flow fields in the reacting cases allowed a coarser resolution. For all test cases, the grid spacing is between 1 and 3 Kolmogorov lengths in all directions. To exclude box-size effects it has been checked that two-point correlations of the velocity components and scalars become small at a separation of half the domain size (see Mahle 2007).

In the reacting cases, one stream of the mixing layer contains oxygen and nitrogen, and the other hydrogen and nitrogen premixed so that the stoichiometric mixture fraction is  $Z_s = 0.3$ . The temperatures of the free streams are chosen such that, at constant pressure, their densities are the same. In the inert cases, pure nitrogen mixes with pure oxygen, which have a similar molecular weight. This results in a nearly constant mean density at constant pressure.

Hydrogen chemistry is simplified and preferential diffusion effects are excluded in order to keep the number of additional variables small: the assumption of one global reaction with infinitely fast reaction rates and a constant common Schmidt number allows their mass fractions to be related to a single scalar, the mixture fraction  $Z$ , the transport equation of which does not contain a source term. In addition to the transport equation of  $Z$ , the continuity equation, the momentum equations, and the energy equation are solved to retain a fully compressible formulation, in which dynamic viscosity and heat conductivity depend on local temperature and species mass fractions. The transport equations are integrated in time using a third-order low-storage Runge–Kutta scheme and sixth-order compact central schemes in space. The primitive variables are filtered every 20 time steps to prevent spurious accumulation of energy in the highest wavenumbers using a sixth-order compact filter.

The inert mixing layers were initialized with hyperbolic tangent profiles for the mean streamwise velocity with superimposed random, broadband fluctuations (maximum amplitude  $0.1\Delta u$ ) for all velocity components, whereas already turbulent velocity fields from the inert mixing layers were used for initializing the reacting ones. The Reynolds numbers at the beginning of the simulations were therefore higher for the reacting mixing layers than for the inert ones—around 12000 vs. 640. These and all Reynolds numbers in the following, if not stated otherwise, are based on the instantaneous vorticity thickness,  $\delta_{\omega}$ ,  $\Delta u$  and on the average density/viscosity of the free streams. For the reacting mixing layers, a hyperbolic tangent profile of the mixture fraction was used for initialization together with a profile of the temperature based on infinitely fast, irreversible chemistry and a Lewis number of 1. This resulted in a linear relation between temperature and mixture fraction and an initial density profile with a shape

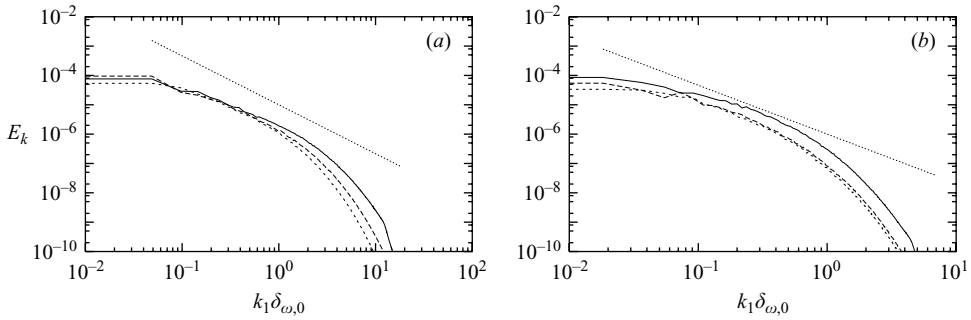


FIGURE 1. One-dimensional streamwise spectra of the turbulent kinetic energy  $\tilde{k}/\Delta u^2$  at the beginning of the self-similar state ( $k_1$  is the wavenumber in the streamwise direction): (a) inert mixing layers, (b) reacting mixing layers. Solid:  $M_c = 0.15$ , dashed:  $M_c = 0.7$ , dotted:  $M_c = 1.1$ . Also shown is a reference line with a slope of  $-5/3$ .

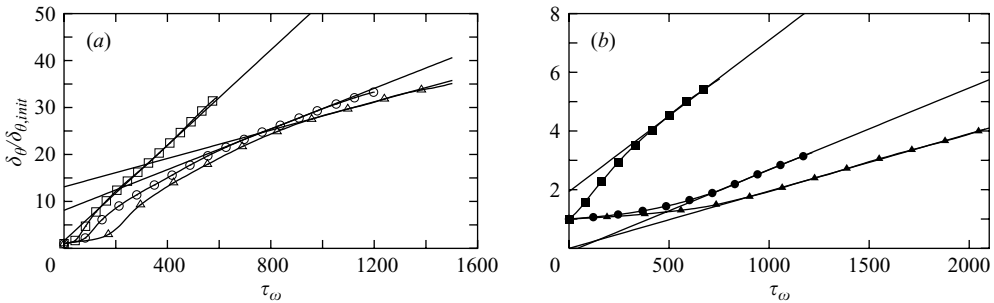


FIGURE 2. Momentum thickness, normalized by its initial value  $\delta_{\theta,init}$ , as a function of  $\tau_{\omega} = t \Delta u / \delta_{\omega,0}$  with physical time  $t$ . (a)  $\square$ , inert-0.15;  $\circ$ , inert-0.7;  $\triangle$ , inert-1.1. (b)  $\blacksquare$ , inf-0.15;  $\bullet$ , inf-0.7;  $\blacktriangle$ , inf-1.1; straight lines show linear regressions for the self-similar state

similar to that of the self-similar state (see § 3.2). All mixing layers rapidly achieved a self-similar state with Reynolds numbers ranging from 15000 to 35000. For Reynolds number based on the local density and viscosity, the values in the centre of the reacting mixing layers are reduced by a factor of about 6. Figure 1 shows the spectra of the turbulent kinetic energy at the beginning of the self-similar state. The energy cascades are well established in all cases. At the highest wavenumbers, the energy falls off smoothly over several orders of magnitude.

In the following, the inert/reacting cases are denoted by inert-XX, respectively inf-XX, where XX represents the convective Mach number.

### 3. Analysis and results

#### 3.1. Momentum thickness growth rates

The stabilizing effect of heat release and compressibility, visible from instantaneous snapshots of the flow field (see Mahle 2007), is also reflected in the temporal evolution of the momentum thickness  $\delta_{\theta}$  which is shown in figure 2 for the inert and reacting test cases. It can be seen that the momentum thickness growth rate reduces with increasing compressibility and with heat release. The mean dilatation due to heat release is small. When a self-similar state is reached, constant momentum thickness growth rates are established as shown by the linear regressions. The ratios of the vorticity thickness and the momentum thickness during the self-similar state are 4.0

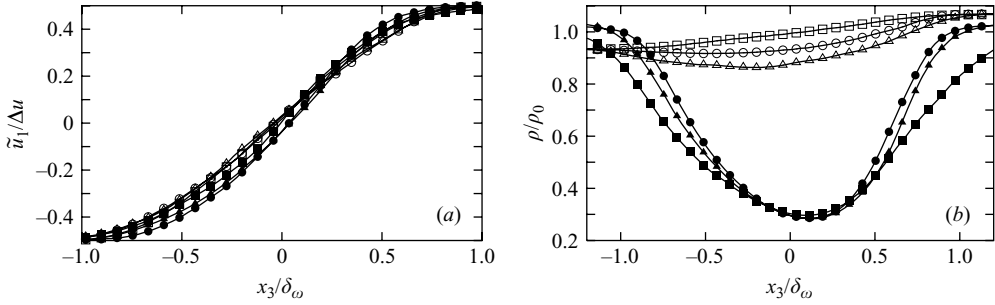


FIGURE 3. (a) Favre averaged streamwise velocity, normalized by  $\Delta u$ . (b) Mean density, normalized by  $\rho_0$ :  $\square$ , inert-0.15;  $\circ$ , inert-0.7;  $\triangle$ , inert-1.1;  $\blacksquare$ , inf-0.15;  $\bullet$ , inf-0.7;  $\blacktriangle$ , inf-1.1.

for cases inert-0.15 and inert-0.7, 4.2 for inert-1.1 and 9.9, 12.5 and 11.5 for cases inf-0.15, inf-0.7 and inf-1.1, respectively. The self-similar state is not only characterized by constant thickness growth rates, but also by a collapse of spatially averaged, normalized profiles of flow variables (see Mahle 2007).

### 3.2. Mean profiles

During the self-similar state, profiles of flow variables, averaged at different times over the homogeneous directions, collapse when non-dimensionalized appropriately. Therefore, temporal averages can be taken, which is done for all normalized profiles in this and the following sections. Figure 3 shows the Favre-averaged streamwise velocity, which is not significantly influenced by compressibility and heat release. In contrast, the mean density is visibly affected by both mechanisms.  $\Delta u = u_1 - u_2$  is the velocity difference across the layer (upper stream: index 1, lower stream: index 2),  $\rho_0 = (\rho_1 + \rho_2)/2$  is the reference density. Here and in the following, an overbar denotes a Reynolds-averaged quantity and a tilde a Favre averaged quantity. Primes and double primes indicate the respective fluctuations. Figure 3 shows that heat release, in particular, reduces  $\bar{\rho}$  strongly due to the high temperatures in the vicinity of the flame sheet. For the inert cases, a decrease of the mean density with increasing  $M_c$  is a result of dissipative heating. When reaction sets in, this mechanism is masked in the centre by the stronger effect of heat release.

### 3.3. Reynolds stresses and turbulent kinetic energy

When neglecting mean viscous effects, the non-dimensional momentum thickness growth rate is given by (see Vreman *et al.* 1996)

$$\delta_\theta = \frac{1}{\Delta u} \frac{d\delta_\theta}{dt} \approx -\frac{2}{\rho_0 \Delta u^3} \int_{-\infty}^{\infty} \overline{\rho u_1'' u_3''} \frac{\partial \tilde{u}_1}{\partial x_3} dx_3. \tag{3.1}$$

This shows that there are two factors that might be responsible for the reduction of the growth rate by compressibility and heat release: the slope of the Favre-averaged streamwise velocity,  $\partial \tilde{u}_1 / \partial x_3$ , and the Reynolds shear stress  $\overline{\rho R_{13}} = \overline{\rho u_1'' u_3''}$ . The first quantity has been shown in figure 3(a) to be similar for all mixing layers under investigation. Therefore, a decrease in Reynolds shear stress must be the main cause for the decrease in growth rate. This is confirmed by figure 4.

The stabilizing effect of heat release and compressibility on turbulent fluctuations can also be seen from the other Reynolds stresses. Consequently, the turbulent kinetic energy,  $\overline{\rho k} = \overline{\rho u_i'' u_i''}$ , which is shown in figure 5, also decreases when normalized in the same way as the Reynolds shear stress. However, when normalizing with the mean

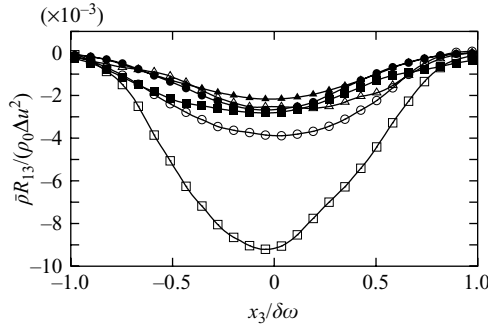


FIGURE 4. Reynolds shear stress  $\bar{\rho}R_{13}$ , normalized by  $\rho_0\Delta u^2$ , symbols as in figure 3.

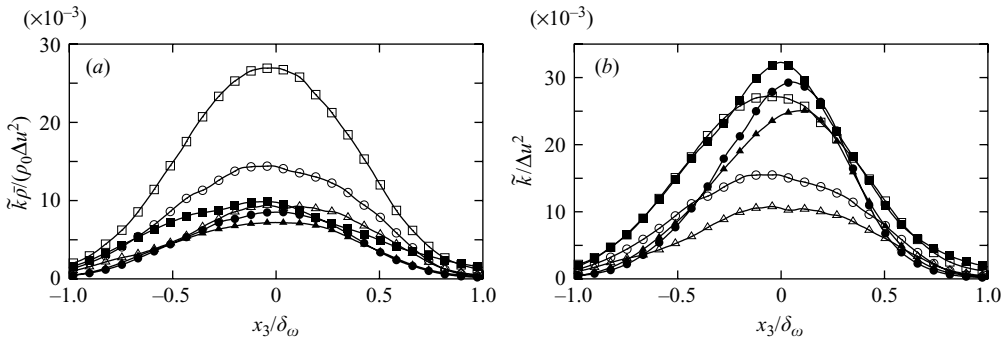


FIGURE 5. Turbulent kinetic energy in different normalizations, symbols as in figure 3.

density  $\bar{\rho}$  instead of the constant reference density  $\rho_0$ , unexpected consequences of heat release appear, namely an increase of  $\tilde{k}$  close to the centre of the shear layer compared to inert flow (figure 5). To understand this behaviour better, we consider the low-Mach-number inert and reacting cases (open and closed symbols, respectively). The reduction of  $\bar{\rho}\tilde{k}$  by heat release in figure 5(a) is a mean density effect, since the two curves collapse in figure 5(b) over most of the domain, except around the centre of the shear layer. The increase of  $\tilde{k}$  due to heat release, there, is a consequence of the increase in correlation between Favre velocity fluctuations, which differs from the correlation between  $\rho u'_i$  and  $u'_i$  (see Mahle 2007). The increase in the value of  $\tilde{k}/\Delta u^2$  in the presence of heat release not only holds at higher Mach number but also increases in magnitude. The effect of compressibility, on the other hand, has only a weak mean density component for the Mach numbers considered, as concluded from figure 3(b). Its stabilizing effect will later be related to the pressure fluctuations and their determining Poisson equation.

### 3.4. Reynolds stress transport equations

The transport equations of the Reynolds stresses are

$$\frac{\partial \bar{\rho}R_{ij}}{\partial t} + \frac{\partial (\bar{\rho}\tilde{u}_k R_{ij})}{\partial x_k} = P_{ij} - \epsilon_{ij} + T_{ij} + \Pi_{ij} + \Sigma_{ij} \tag{3.2}$$

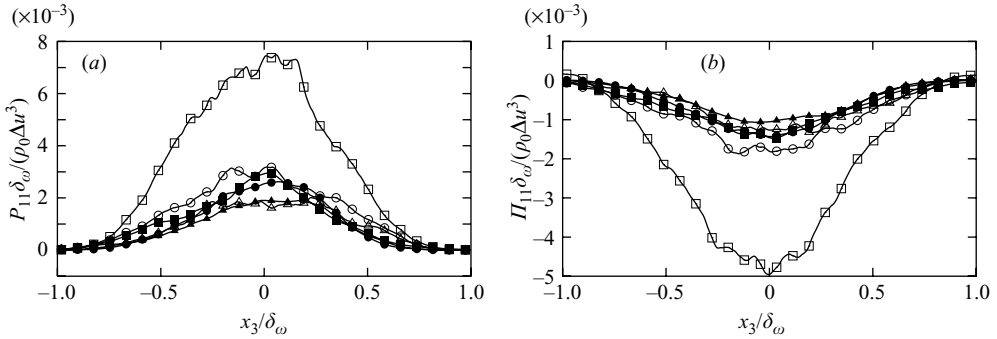


FIGURE 6. Production rate (a) and pressure–strain rate (b) of streamwise Reynolds stress, normalized by  $\rho_0 \Delta u^3 / \delta_\omega$ , symbols as in figure 3.

with the production rates  $P_{ij}$ , the dissipation rates  $\epsilon_{ij}$ , the turbulent transport terms  $T_{ij}$ , the pressure–strain correlations  $\Pi_{ij}$  and the mass flux coupling terms  $\Sigma_{ij}$ . The influence of compressibility and heat release on the production and pressure–strain tensors,

$$P_{ij} = - \left( R_{ik} \frac{\partial \tilde{u}_j}{\partial x_k} + R_{jk} \frac{\partial \tilde{u}_i}{\partial x_k} \right), \quad \Pi_{ij} = \overline{p' \left( \frac{\partial u''_i}{\partial x_j} + \frac{\partial u''_j}{\partial x_i} \right)} = 2 \overline{p' s''_{ij}}, \quad (3.3)$$

is particularly strong. The production and the pressure–strain rate terms of the streamwise Reynolds stress  $\bar{\rho} R_{11}$  are shown in figure 6 normalized by  $\rho_0, \Delta u$  and  $\delta_\omega$ . Both compressibility and heat release strongly attenuate production and redistribution of fluctuating kinetic energy. A similar reduction can be observed for the pressure–strain rates of the other diagonal Reynolds stresses, with the consequence that the redistribution from the streamwise Reynolds stress to the other diagonal ones is hampered by compressibility and heat release. A direct consequence of the reduced streamwise pressure–strain correlation with compressibility is the reduced momentum thickness growth rate as shown by Vreman *et al.* (1996) and Freund *et al.* (2000) for inert mixing layers. In Mahle (2007), such an equation,

$$\delta_\theta = \frac{-\tilde{\Pi}_{11} / (\rho_0 \Delta u^3) + K_\epsilon}{1 - K_{11}}, \quad (3.4)$$

is shown to be valid for both inert and reacting mixing layers at convective Mach numbers up to  $M_c = 1.1$ . In (3.4),  $\tilde{\Pi}_{11}$  is the streamwise pressure–strain rate integrated in the direction of the shear.  $K_{11}$  and  $K_\epsilon$  are related to the streamwise Reynolds stress and its dissipation rate, and they change much less between cases than  $\tilde{\Pi}_{11}$  as shown in Mahle (2007).

### 3.5. Reduction of pressure–strain correlations

The described attenuation of pressure–strain correlations,  $\Pi_{ij}$ , by compressibility and heat release can be traced back to the attenuation of pressure fluctuations (see figure 7) which is found to be stronger than the reduction of pressure fluctuating velocity gradients and of their correlation coefficients. In order to explain the reduction of the pressure fluctuations and the pressure–strain correlations  $\Pi_{ij}$  in temporally evolving mixing layers, an equation determining  $p'$  is obtained by taking the divergence of the momentum equation, introducing the continuity equation and subtracting the averaged resulting equation. Taking the mean flow homogeneity in streamwise and

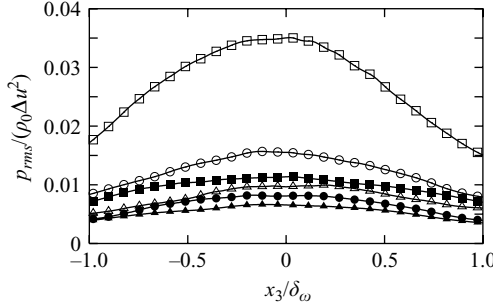


FIGURE 7. R.m.s. value of pressure fluctuations, normalized by  $\rho_0 \Delta u^2$ , symbols as in figure 3.

spanwise directions into account, we obtain

$$\begin{aligned}
 \frac{\partial^2 p'}{\partial x_j^2} = & \underbrace{-\bar{\rho} \frac{\partial^2}{\partial x_i \partial x_j} (u_i'' u_j'' - \overline{u_i'' u_j''})}_{A_1} \underbrace{-2\bar{\rho} \frac{\partial \tilde{u}_1}{\partial x_3} \frac{\partial u_3''}{\partial x_1}}_{A_2} \underbrace{-2\bar{\rho} \frac{\partial \tilde{u}_3}{\partial x_3} \left( \frac{\partial u_1''}{\partial x_1} + \frac{\partial u_2''}{\partial x_2} + 2 \frac{\partial u_3''}{\partial x_3} \right)}_{A_3} \underbrace{-2\bar{\rho} \frac{\partial^2 \tilde{u}_3}{\partial x_3^2} u_3''}_{A_4} \\
 & \underbrace{-2 \frac{\partial \bar{\rho}}{\partial x_3} \frac{\partial}{\partial x_j} (u_3'' u_j'' - \overline{u_3'' u_j''})}_{B_1} \underbrace{-\frac{\partial^2 \bar{\rho}}{\partial x_3^2} (u_3''^2 - \overline{u_3''^2})}_{B_2} \underbrace{-4u_3'' \frac{\partial \bar{\rho}}{\partial x_3} \frac{\partial \tilde{u}_3}{\partial x_3}}_{B_3} \underbrace{-2 \frac{\partial \tilde{u}_1}{\partial x_3} \frac{\partial}{\partial x_1} (\rho' u_3'')}_{C_1} \\
 & \underbrace{-\frac{\partial^2}{\partial x_i \partial x_j} (\rho' u_i'' u_j'' - \overline{\rho' u_i'' u_j''})}_{C_2} \underbrace{-2 \frac{\partial \tilde{u}_3}{\partial x_3} \left( \frac{\partial}{\partial x_1} (\rho' u_1'') + \frac{\partial}{\partial x_2} (\rho' u_2'') + 2 \frac{\partial}{\partial x_3} (\rho' u_3'') \right)}_{C_3} \\
 & \underbrace{-2\rho' \left( \frac{\partial \tilde{u}_3}{\partial x_3} \right)^2}_{C_4} \underbrace{-2\rho' u_3'' \frac{\partial^2 \tilde{u}_3}{\partial x_3^2}}_{C_5} \underbrace{+ \frac{\overline{D^2 \rho'}}{\overline{Dt^2}}}_{C_6} \underbrace{+ \frac{\partial^2 \tau'_{ij}}{\partial x_i \partial x_j}}_D
 \end{aligned} \tag{3.5}$$

with the boundary condition  $\partial p' / \partial x_3 = 0$  at  $\pm L_3/2$ . Although (3.5) is valid for inert and reacting mixing layers, below we analyse it, for reacting layers only, since pressure fluctuations of all the reacting flows are smaller than those of the nearly incompressible inert mixing layer (see figure 7). The terms on the right-hand side of (3.5) can be grouped into four categories. The *A*-terms depend on the mean density. It will be shown in the following that the most important ones are  $A_1$  and  $A_2$ . The other, i.e. the *B*-, *C*- and *D*-terms, are only present in compressible or reacting flows and involve density and viscous stress fluctuations. Term *D*, which is the second derivative of the fluctuating stress tensor,  $\tau'_{ij}$ , turns out to be very small for the cases studied in this work and can therefore be neglected. Term  $C_6$  contains pressure fluctuations as well as an explicit contribution of the heat release term for reacting flows:

$$\frac{D^2 \rho'}{Dt^2} = \frac{1}{\bar{c}^2} \frac{D^2 p'}{Dt^2} - \frac{1}{c_p T} \frac{DQ'}{Dt} + \text{h.o.t.}, \tag{3.6}$$

where  $c$  denotes the sonic speed and  $c_p$  the heat capacity of the gas mixture at constant pressure.  $Q'$  denotes fluctuations of the heat release term  $Q$ ,

$$Q = - \sum_{\alpha} \rho h_{\alpha} \frac{DY_{\alpha}}{Dt} \tag{3.7}$$



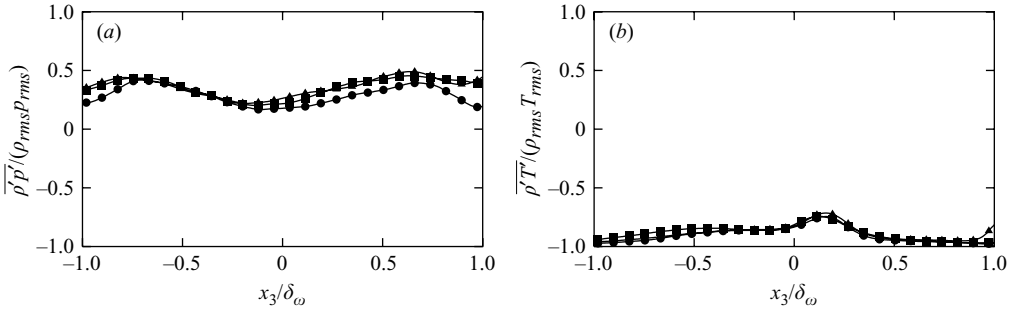


FIGURE 8. Density–pressure (a) and density–temperature (b) correlation coefficients: ■, inf-0.15; ●, inf-0.7; ▲, inf-1.1.

with  $h_\alpha$  being the enthalpy of species  $\alpha$  and  $DY_\alpha/Dt$  the substantial derivative of its mass fraction  $Y_\alpha$ . In contrast to the inert mixing layers (see Pantano & Sarkar 2002), the correlation coefficient between density and pressure fluctuations is below 0.5 and the density–temperature correlation is close to  $-1$  (figure 8) which is to be expected for sufficiently high heat release. This indicates that isentropic effects are small. Hence the first term on the right-hand side of (3.6) is neglected. This approximation is justified by the precision of the results obtained in the following (see figures 9b and 10b).

Equation (3.5) then becomes a Poisson equation,

$$\frac{\partial^2 p'}{\partial x_j^2} = f \tag{3.8}$$

with all terms on the right-hand side of (3.5) summarized in the source term  $f$ . After performing a Fourier transformation in the homogeneous directions,  $p(x_1, x_2, x_3) \rightarrow \hat{p}(k_1, k_2, x_3)$ , and a coordinate transformation in the direction of the main shear,  $\check{x}_3 = 2x_3/L_3$ , (3.8) becomes

$$\left( \frac{d^2}{d\check{x}_3^2} - k_1^2 - k_2^2 \right) \hat{p}(k_1, k_2, \check{x}_3) = \hat{f}(k_1, k_2, \check{x}_3) \quad \text{with} \quad \frac{\partial \hat{p}}{\partial \check{x}_3} \Big|_{\check{x}_3=\pm 1} = 0. \tag{3.9}$$

This equation can be solved with a Green’s function  $G$  (see Kim 1989),

$$p'(x_1, x_2, \check{x}_3) = \int_{-1}^1 G * f(x_1, x_2, \check{x}_3) d\check{x}_3, \tag{3.10}$$

where the convolution  $G * f$  represents the inverse Fourier transform of  $\hat{G}\hat{f}$ . Multiplication with  $2s''_{ij}$  and statistical averaging results in the pressure–strain correlations

$$\Pi_{ij}(\check{x}_3) = 2 \int_{-1}^1 G * f(x_1, x_2, \check{x}_3) s''_{ij}(x_1, x_2, \check{x}_3) d\check{x}_3. \tag{3.11}$$

By inserting only part of the right-hand side  $f$  into (3.8), e.g. term  $A_1$ , it is possible to see which of the terms contributes most to the reduction of the pressure–strain correlation.

Figure 9(a) shows the contributions to the pressure–strain term  $\Pi_{11}$  for case inf-0.15. The contributions from terms  $A_1$  and  $A_2$ , which depend on the mean density, are the largest; the other contributions, though non-zero, are smaller. This is also the case for term  $C_6$ , which contains the heat release term explicitly. Despite neglecting acoustic effects, the summation of all terms that are shown in figure 9(a) provides a



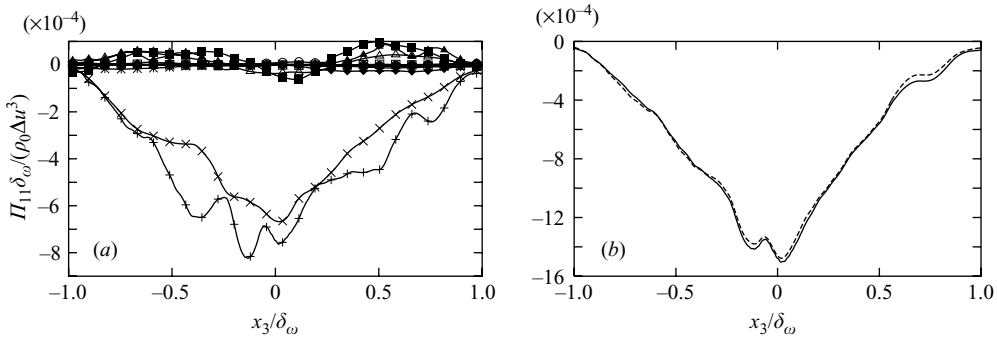


FIGURE 9. Case inf-0.15. (a) Parts of the pressure–strain correlation  $\Pi_{11}$  computed with the Green’s function. +,  $f = f(A_1)$ ; x,  $f = f(A_2)$ ; \*,  $f = f(A_3)$ ; □,  $f = f(A_4)$ ; ■,  $f = f(B_1)$ ; ○,  $f = f(B_2)$ ; ●,  $f = f(B_3)$ ; △,  $f = f(C_1)$ ; ▲,  $f = f(C_2)$ ; ▽,  $f = f(C_3)$ ; ▼,  $f = f(C_4)$ ; ◇,  $f = f(C_5)$ ; ◆,  $f = f(C_6)$ . (b) Pressure–strain correlation  $\Pi_{11}$ . Solid: computed with the help of the Green’s function with  $f = f(\sum_{i=1}^4 A_i + \sum_{i=1}^3 B_i + \sum_{i=1}^6 C_i)$ , dashed: evaluated directly.

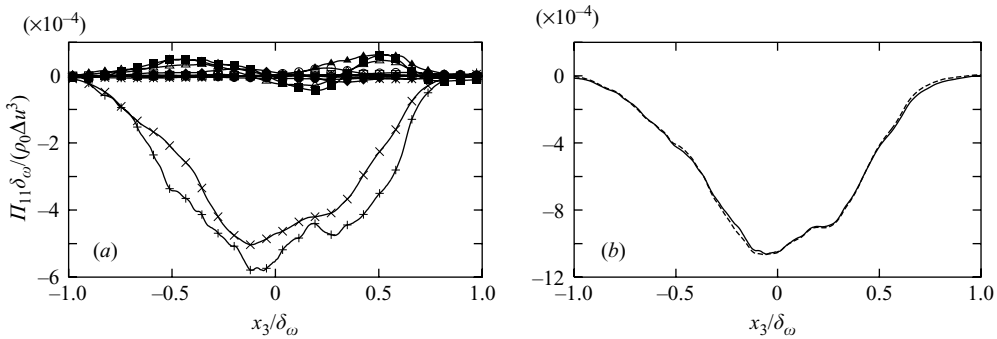


FIGURE 10. Case inf-1.1. (a) Parts of the pressure–strain correlation  $\Pi_{11}$  computed with the Green’s function. Symbols as in Fig. 9(a). (b) Pressure–strain correlation  $\Pi_{11}$ . Lines as in figure 9(b).

good approximation to  $\Pi_{11}$  (see figure 9b). Figure 10 provides a similar analysis for case inf-1.1 with comparable results.

To find whether the reduction of the pressure–strain correlation  $\Pi_{11}$  by heat release (see figure 6b) is a consequence of the reduced mean density (see figure 3), which appears as a factor in terms  $A_1$  and  $A_2$ ,  $\rho_0$  instead of  $\bar{\rho}$  is inserted into the terms on the right-hand side of (3.5). Density fluctuations are ignored. Figure 11 shows the resulting contributions to  $\Pi_{11}$  for case inf-0.15: compared to figure 9(a), the contributions from terms  $A_1$  and  $A_2$  have increased significantly. The total pressure strain rate has now approximately the same size as for the inert case at  $M_c = 0.15$ . Since similar observations can be made for all pressure–strain correlations evaluated with constant  $\rho_0$ , it can be concluded that the reduction of  $\Pi_{ij}$  by heat release is predominantly a mean density effect.

#### 4. Summary and conclusions

DNS of inert and reacting compressible mixing layers have been performed at convective Mach numbers  $M_c = 0.15, 0.7, 1.1$  and Reynolds numbers from 15000 to 35000 during periods of self-similar turbulence. It was found that the effects of compressibility and heat release influence temporally evolving mixing layers in a

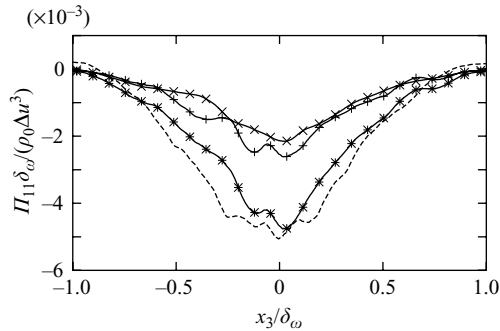


FIGURE 11. Case inf-0.15. Parts of the pressure–strain correlation  $\Pi_{11}$  computed with the Green’s function and assuming constant density  $\rho_0$ , +,  $f = f(A_1)$ ; ×,  $f = f(A_2)$ ; \*,  $f = f(A_1 + A_2)$ . Dashed line shows  $\Pi_{11}$  for case inert-0.15 (where the mean density change is small) as obtained directly from DNS data.

globally similar fashion: momentum thickness growth rates, Reynolds shear stresses, their production rates and pressure–strain correlations are reduced when convective Mach numbers rise and/or chemical reactions set in. The physical mechanisms underlying the behaviour of inert and reacting mixing layers are, however, different. In the Mach number range investigated, the reduction of the turbulent kinetic energy and the Reynolds stresses by heat release is primarily due to the strong decrease of mean density around the flame sheet and therefore mainly a mean density effect. While density and temperature fluctuations increase, pressure fluctuations are strongly attenuated by heat release and decrease further with the convective Mach number. Because, for the reacting mixing layers, the correlation coefficient between density and temperature fluctuations is close to  $-1$  and the density–pressure correlation is below 0.5, the direct coupling between density and pressure fluctuations is weak. Hence, a Poisson equation for the pressure fluctuations can be solved to obtain the pressure fluctuations in reacting mixing layers with the help of a Green’s function for parallel shear flow and to compute the pressure–strain correlations in remarkably good agreement with DNS data.

#### REFERENCES

- FOYSI, H., SARKAR, S. & FRIEDRICH, R. 2004 Compressibility effects and turbulence scaling in supersonic channel flow. *J. Fluid Mech.* **509**, 207–216.
- FREUND, J. B., LELE, S. K. & MOIN, P. 2000 Compressibility effects in a turbulent annular mixing layer. part 1. turbulence and growth rate. *J. Fluid Mech.* **421**, 229–267.
- HERMANSON, J. & DIMOTAKIS, P. 1989 Effects of heat release in a turbulent, reacting shear layer. *J. Fluid Mech.* **199**, 333–375.
- KIM, J. 1989 On the structure of pressure fluctuations in simulated turbulent channel flow. *J. Fluid Mech.* **205**, 421–451.
- MAHLE, I. 2007 Direct and large-eddy simulation of inert and reacting compressible turbulent shear layers. PhD thesis, Technische Universität München, Germany.
- McMURTRY, P., RILEY, J. & METCALFE, R. 1989 Effects of heat release on the large-scale structure in turbulent mixing layers. *J. Fluid Mech.* **199**, 297–332.
- MILLER, M. F., BOWMAN, C. T. & MUNGAL, M. G. 1998 An experimental investigation of the effects of compressibility on a turbulent reacting mixing layer. *J. Fluid Mech.* **356**, 25–64.
- PANTANO, C. & SARKAR, S. 2002 A subgrid model for nonlinear functions of a scalar. *J. Fluid Mech.* **451**, 329–371.
- PANTANO, C., SARKAR, S. & WILLIAMS, F. A. 2003 Mixing of a conserved scalar in a turbulent reacting shear layer. *J. Fluid Mech.* **481**, 291–328.
- VREMAN, A. W., SANDHAM, N. D. & LUO, K. H. 1996 Compressible mixing layer growth rate and turbulence characteristics. *J. Fluid Mech.* **320**, 235–258.